

Tunable Microwave Conductance of Nanodomains in Ferroelectric $\text{PbZr}_{0.2}\text{Ti}_{0.8}\text{O}_3$ Thin Film

Stuart R. Burns,* Alexander Tselev, Anton V. Ievlev, Joshua C. Agar, Lane W. Martin, Sergei V. Kalinin, Daniel Sando, and Petro Maksymovych*

Ferroelectric materials exhibit spontaneous polarization that can be switched by electric field. Beyond traditional applications as nonvolatile capacitive elements, the interplay between polarization and electronic transport in ferroelectric thin films has enabled a path to neuromorphic device applications involving resistive switching. A fundamental challenge, however, is that finite electronic conductivity may introduce considerable power dissipation and perhaps destabilize ferroelectricity itself. Here, tunable microwave frequency electronic response of domain walls injected into ferroelectric lead zirconate titanate ($\text{PbZr}_{0.2}\text{Ti}_{0.8}\text{O}_3$) on the level of a single nanodomain is revealed. Tunable microwave response is detected through first-order reversal curve spectroscopy combined with scanning microwave impedance microscopy measurements taken near 3 GHz. Contributions of film interfaces to the measured AC conduction through subtractive milling, where the film exhibited improved conduction properties after removal of surface layers, are investigated. Using statistical analysis and finite element modeling, we inferred that the mechanism of tunable microwave conductance is the variable area of the domain wall in the switching volume. These observations open the possibilities for ferroelectric memristors or volatile resistive switches, localized to several tens of nanometers and operating according to well-defined dynamics under an applied field.

information is stored in the polarization orientation. A recent resurgence of interest in electronic properties of ferroelectrics, such as polarization controlled tunneling and conductivity of domain walls, potentially enables a new generation of applications utilizing resistive probes of polarization state, such as synaptic junctions,^[1–5] domain-wall resistors, and domain-wall logic.^[6–9] At the same time, ferroelectric control over resistive switching may enable neuromorphic devices without structural phase change and filamentary breakdown, potentially leading to much higher energy efficiency.

One of the key properties enabling the coupling of ferroelectric and resistive switching is the electronic conductivity of domain walls,^[10] which was experimentally demonstrated in numerous materials,^[11–14] beginning with the work of Seidel et al.^[15] The intrinsic coupling of domain walls to applied electric field, their nanoscale dimensions, and the flexibility afforded by deterministic control of ferroelectric, ferroelastic, and ferromagnetic structures

containing conducting domain walls^[16–20] provide great promise for new memory and electronics-engineering concepts, such as racetrack memories^[21] or magnetoelectric spin-orbit devices.^[22] A notable challenge on the path of ferroresistive switching is that metallic conductivity and ferroelectricity are fundamentally


1. Introduction

Ferroelectric materials have long been pursued for use in non-volatile memory and logic applications. Polarization switching has been employed in capacitive ferroelectric memories, where

S. R. Burns, D. Sando
School of Materials Science and Engineering
University of New South Wales
Sydney 2052, Australia
E-mail: stuart.burns@unsw.edu.au

S. R. Burns
Department of Chemistry
University of Calgary
Calgary AB T2N 1N4, Canada

A. Tselev
CICECO-Aveiro Institute of Materials and Department of Physics
University of Aveiro
Aveiro 3810-193, Portugal

 The ORCID identification number(s) for the author(s) of this article can be found under <https://doi.org/10.1002/aelm.202100952>.

DOI: 10.1002/aelm.202100952

A. V. Ievlev, S. V. Kalinin, P. Maksymovych
Centre for Nanophase Materials Sciences
Oak Ridge National Laboratory
Oak Ridge, TN 37831, USA
E-mail: maksymovychp@ornl.gov

J. C. Agar, L. W. Martin
Department of Materials Science and Engineering
University of California, Berkeley
Berkeley, CA 94720, USA

J. C. Agar
Department of Material Science and Engineering
Lehigh University, Bethlehem
PA 18015, USA

L. W. Martin
Materials Sciences Division
Lawrence Berkeley National Laboratory
Berkeley, CA 94720, USA

opposed.^[23,24] In turn, it is highly nontrivial to establish good electrical contact to the domain wall.^[25] In fact, charged domain walls may reconstruct in the contact region preventing good metallic contact from being established on an intrinsic level.^[26] The other fundamental issue is that domain-wall conductivity increases with increasing charge of the domain wall, but so does the domain-wall energy,^[27] which ultimately requires unique approaches to creating strongly conductive domain walls. Meanwhile, increasing carrier density in the bulk by doping/alloying is also complicated and may eventually suppress ferroelectric ordering.^[28]

An alternative regime to measure electronic properties of ferroelectric domain walls relies on high-frequency AC regimes.^[29] High-frequency AC conductance effectively shorts the Schottky barrier, making highly resistive contacts required for ferroelectric switching compatible with an electronic read-out of the ferroelectric state.^[30,31] This mechanism is complementary to a recently demonstrated photovoltaic read-out of the ferroelectric state, which likewise circumvents the need for Ohmic contacts.^[32]

Here, we report the observation of tunable electronic properties of ferroelectric switching at microwave frequencies and on the level of a single ferroelectric nanodomain. Utilizing a scanning probe as a top electrode, we locally switched the domain structure of a thin $\text{PbZr}_{0.2}\text{Ti}_{0.8}\text{O}_3$ (PZT) film.^[33,34] Through a combination of first-order reversal curve (FORC) spectroscopy, which creates nanodomains in sub-100 nm regions of the ferroelectric film and probes their evolution, and simultaneous piezoresponse force (PFM) and scanning microwave impedance microscopy (sMIM) measurements, we captured the evolution and dynamics of the ferroelectric state. The results reveal tunable microwave conductance states encoded by the wall's size

and effective density under the probe tip. These results point to memristive behavior from a single ferroelectric nanodomain and are supported by finite-element simulations based upon Landau–Ginzburg–Devonshire theory. Furthermore, subtractive lithography^[35] was applied to probe the sensitivity of tunable microwave conductance in relation to film thickness of the ferroelectric, finding enhancement of microwave conductance in the desired ultrathin limit. Tunable microwave conductance defined by effective domain-wall density may facilitate the realization of ferroelectric memristive devices at microwave frequencies that remain primarily insulating in the DC regime. Power dissipation in such devices would ideally be minimized to capacitive and dielectric effects—potentially shifting the switching power of such devices into the femto- or even attojoule regime.^[36] At the same time, the microwave probe provides new nanoscale insights into the ferroelectric-switching process, extending previous observations of microwave domain-wall conductance^[29,30,37] to ferroelectric dynamics in an electric field.

2. Results and Discussion

Simultaneous sMIM and PFM spectroscopies were carried out while locally switching domains using an applied electric field. **Figure 1a** shows a generic scenario for domain-wall nucleation and local switching under the nanoscale probe. The conductive AFM probe acts as the top electrode in a capacitor geometry. Above a critical electric field, the polarization begins to switch directly under the probe. The colors show the evolution of the polarization nanodomain as a function of time, showing its

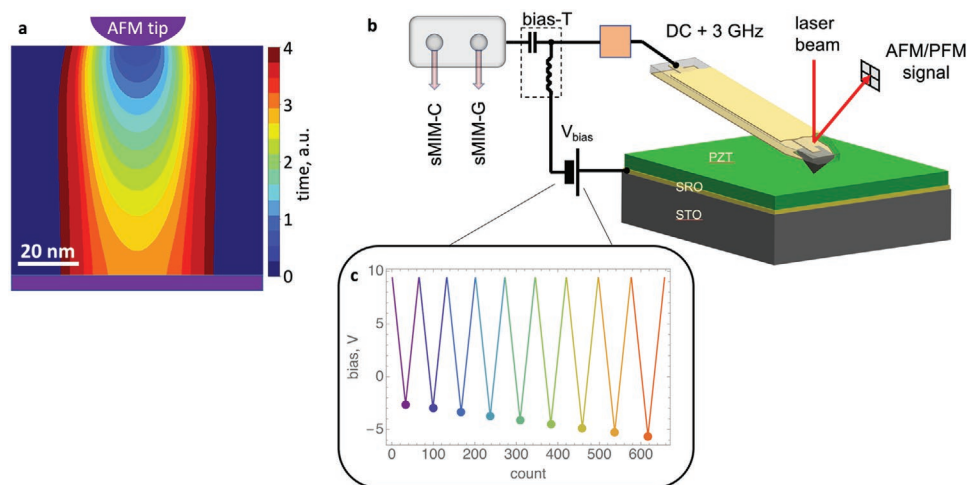


Figure 1. Schematic of the measurement of tunable microwave conductance of ferroelectric domain walls. a) Nucleation and growth of a single nanodomain in localized electric field of a nanoscale capacitor. Colors identify the shape of the nanodomain cross-section calculated as a function of time following nucleation. The domain wall of the nanodomain immediately following nucleation assumes the shape of a prolate half-spheroid. As the domain grows, the spheroid continues to elongate, eventually traversing the film thickness to become cylindrical. b) Schematic of a scanning microwave measurement set-up used to characterize nanodomains. A voltage-biased shielded probe terminating a half-wave resonator is used to apply a local electric field to a thin PZT ferroelectric film and to probe ferroelectric properties through the amplitude and phase of the microwaves reflected from the probe. The latter are translated into variations of capacitance (sMIM-C) and conductance (sMIM-G) of the probe-sample system by accompanying system calibration. c) The probe voltage bias waveform implements a first order reversal curve (FORC) measurement, wherein the system state is probed as a function of increasing turning voltage (V_{turn} – marked by a dot) in a sequence of linear voltage sweeps. The range of V_{turn} is chosen to precede, coincide, and exceed the switching voltage for the ferroelectric polarization in the film, thereby probing single (or few) nanodomains nucleating and growing under the probe.

progressive growth through the depth of the film (perpendicular growth), and eventually, the expanding domain sidewalls (lateral growth) toward formation of a cylindrical domain.

The system under study is presented schematically in Figure 1b. The $\text{PbZr}_{0.2}\text{Ti}_{0.8}\text{O}_3/\text{SrRuO}_3/\text{SrTiO}_3$ (001) (PZT/SRO/STO) heterostructure (the Experimental Section) is characterized by a shielded sMIM probe in contact with the top surface. The sMIM probe acts as a lumped element terminating a half-wave resonator. sMIM data are collected from two decoupled signal channels, namely sMIM-G (conductance) and sMIM-C (susceptance or capacitance). Preliminary testing to separate the contribution of applied biases—AC low-frequency (driving PFM, on the order of kHz), AC high-frequency (driving sMIM, on the order of GHz), and DC (driving the local domain switching)—indicated that the corresponding spectra did not suffer from cross-coupling with other probing potentials.

Further details on the sMIM apparatus and similar experimental configurations can be found elsewhere.^[30,38,39]

FORC switching spectroscopy was applied to probe the switching scenario and track the growing nanodomains' properties in the microwave regime. The distinctive trait of the FORC waveform is the iteratively changing negative bias limit with each cycle, which we refer to as the turning bias, V_{turn} , highlighted by the dot marker on the waveform in Figure 1c. This waveform probes nanodomains in the three regimes of the switching process: prior to, during, and following the coercive field being reached by applied DC bias.

PFM and sMIM FORC spectroscopy results (collected simultaneously) are presented in Figure 2. Minor hysteresis loops along the FORC are observed in both sMIM (Figure 2a,b) and PFM channels (Figure 2c). The ferroelectric switching is initiated in the approximate window from -2.5 to -3.5 V depending

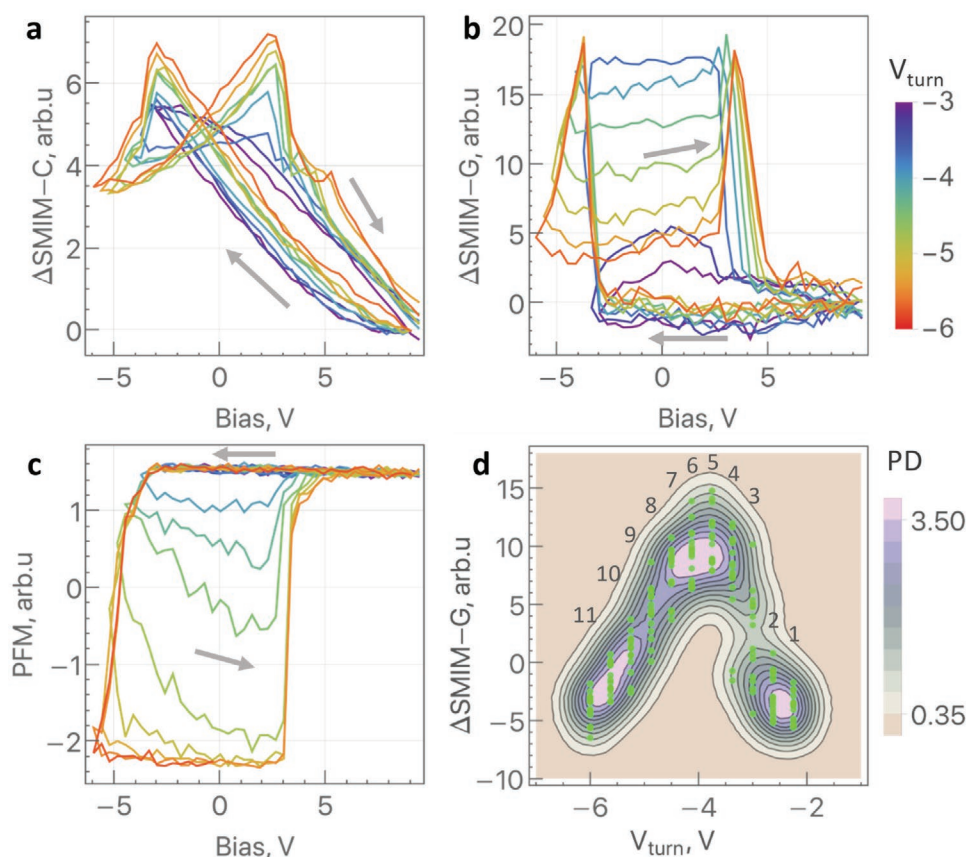


Figure 2. Observation of tunable microwave conductance of ferroelectric nanodomains. First-order reversal measurements for a) microwave capacitance (sMIM-C), b) microwave conductance (sMIM-G), and c) piezoresponse. The arrows point to the direction of voltage cycles. All three signals register onset of ferroelectric switching at a bias of ≈ -3.5 V. The sMIM-C signal is dominated by the tunability of the dielectric constant, whereas sMIM-G reveals tunable microwave conductance. The value of the microwave conductance rapidly increases immediately following switching (at -3.5 V) and then begins to revert to a lower value with increasing size of the ferroelectric domain. Intriguingly, the conductance again proceeds through the maximum along the reverse-switching direction. By controlling the degree of partial switching with the turning voltage (V_{turn}) the microwave conductance at 0 V can be nearly continuously tuned. The colors in (a), (b), and (c) correspond to the turning voltages (V_{turn}), as shown in the colorbar next to (b). d) Statistics accumulated from the switching process for more than ten sequential FORC measurements. The data points (green dots) correspond to sMIM-G signal at 0 V as a function of increasing magnitude of V_{turn} . The probability distribution shown as a contour plot was estimated as a mixture distribution of Gaussian kernels fit to the data-points. The standard deviation of each Gaussian was determined to be ≈ 0.24 , under the constraint that it includes on average ten measured points. The distribution shows approximate confidence limits of the microwave conductance tunability and very good reproducibility of the tunability between randomly sampled locations on the surface of the PZT film. The colorbar is the probability density (PD). Panel d shows data collected from voltage cycles 1 to 11 (marked next to data), whereas, for clarity, panels (a), (b), and (c) only present cycles 3 to 11, as the first 3 cycles are near identical.

on specific location on the surface. The switching processes are detected by rapid variation of all the measured signals in Figure 2. However, each signal reveals its own characteristic trend. Both capacitance and conductance achieves peak value at the forward and the reverse switching events (Figure 2a,b). However, they are different with respect to the bias change around the switching events. The capacitance shows little remanence around 0 V, regardless of the specific value of V_{turn} . In other words, it does not have a strong memory of the degree of switching. By contrast, conductance reveals a series of plateaus between the switching events (Figure 2b), whose value strongly depends on V_{turn} (Figure 2b,d). This observation suggests that with even finer bias increments a potentially quasi-continuous multilevel conductance states can be read-out from a single switching event. Figure 2c clearly points to the ferroelectric origin of the metastable states responsible for tunable conductance, since they emerge during partial ferroelectric switching. We have not yet explored the temporal stability of these states. Given the timescale of the experiment, the states have a lifetime of at least a few seconds. Larger domains nucleated under the tip shown below are stable on much longer timescales in this film. Finally, Figure 2d confirms the repeatability of these results—each point at a given V_{turn} value corresponds to a set of data collected in a different region of the PZT film. The contour plot superimposed on these data points was calculated by a kernel mixture distribution fit, describing the confidence of the conductance signal at a given V_{turn} bias. Given the relatively limited sampling, the finer structure of the distribution (e.g., the “blob” feature between -2 and -3 V) is of no significance yet. However, the overall strong dependence of microwave conductance (measured at zero DC bias) on V_{turn} is statistically reproducible.

To gain deeper insight into the origins of tunable microwave conductance and to probe its dependence on the structure of the film, we employed an inverse lithography approach outlined by Ievlev et al.^[35] Specifically, we carried out bombardment of the film with O_2^- ions to cause progressive removal of the top layers. The sputtering process is performed simultaneously with time-of-flight secondary ion mass spectroscopy chemical characterization to monitor the stoichiometry of the top surface layer. In addition to the reduction in thickness, this process removes (or significantly reduces the influence of) an amorphous top layer which negatively impacts the piezoelectric properties of the film.^[35]

Figure 3a displays an sMIM-G image of the PZT film milled down to 75 nm thickness (from an original 100 nm; see images for other films in Figure S1, Supporting Information). An arrangement of domain walls was created by applying a bias sweep at 4×4 points in a predetermined grid. The “doughnut” shape apparent from the sMIM-G images indicates that, at 3 GHz, the conductance of the domain walls is higher than that of the surrounding domains. sMIM-C images on the other hand do not reveal contrast from domain walls (Figure S2, Supporting Information), which points to electronic origin of microwave conductance.^[30] The average of the spectra collected during this applied bias (from -10 to 10 V in a triangular waveform) are shown in Figure 3b. The spectra feature conductance peaks, similar to the FORC measurements in Figure 2b. Combined with imaging, these data show that sMIM-G conductance

peaks at the polarization switching events are mainly contributed to by domain walls. By extension, tunable microwave conductance is also underpinned by the properties of ferroelectric nanodomains mediating the switching process, rather than for example motion of adsorbates. Meanwhile, the sensitivity of the effect to detailed surface conditions is not large. In fact, the average sMIM-G spectra are less noisy upon decreased thickness and exhibit larger signal (Figure 3c). It is likely that the signal improves by removing top layer, defects, or adsorbates accumulated over time in the as-grown film.^[40]

Figure 3c summarizes the conductance signals by comparing their corresponding distributions obtained from sMIM images and spectra. To ascertain systematic comparison of different regions of the sample, the conductance signals observed for domain walls (in sMIM-G images and sMIM-G spectra) were normalized by subtracting the values outside the domain walls in images and away from switching events in spectra (this was done on each individual measurement prior to averaging). The contributions to the sMIM-G signal are denoted by s.#, w.#, and d.#, where s, w, and d represent spectra (extracted from data similar to that shown in Figure 3b), walls (signal extracted from domain wall regions in sMIM images similar to in Figure 3a), and domains (the background signal from sMIM images), respectively. The thickness of the sample in the region is denoted by #. The violin diagrams in Figure 3c depict the experimental distribution of the measured values, which is quite broad owing to an expected stochastic distribution of defects in the film. Notably, microwave conductance of domain walls measured by imaging (Figure 3a) and peak values from spectroscopy (Figure 3b) are comparable, with values in spectroscopy at most a factor of two larger. This observation reaffirms the conclusion that injected domain walls are the principal contributor of tunable conductance in switching spectroscopy, as compared to impurities, surfaces, and other factors (though their influence cannot be completely ruled out). A second observation is that there is a general trend of an increase of sMIM-G signal with decreasing thickness (Figure 3d). If we treat the domain wall as a conductor, a basic interpretation of this result could be the domain wall acting as a conducting filament—the conductance decreases with increasing domain wall length between electrodes and is therefore notably smaller in thicker regions of the film.

Distinctly observable tunable sMIM-G conductance can emerge from several complementary phenomena. An important feature of Figure 3b is that the peak conductance of the nanodomain junction is observed between the point at which polarization first switches at ≈ -3.5 V, and the point before it back-switches at $\approx +3$ V, which is uniquely revealed by the FORC measurement, and echoes an earlier similar measurement using conductive AFM at DC.^[41] This property not only enhances the prospects of tuning the junction by either bias polarity, but also fundamentally implies that the junction exhibits reversible ferroelectric switching properties. In particular, the configuration of the injected domain wall that maximizes conductance at negative bias polarity is first impeded by increasing negative bias but can be restored by appropriate positive polarity. The simplest picture would correspond to a polar nanodomain that first increases in dimensions and then decreases, retracting roughly to the same overall shape.

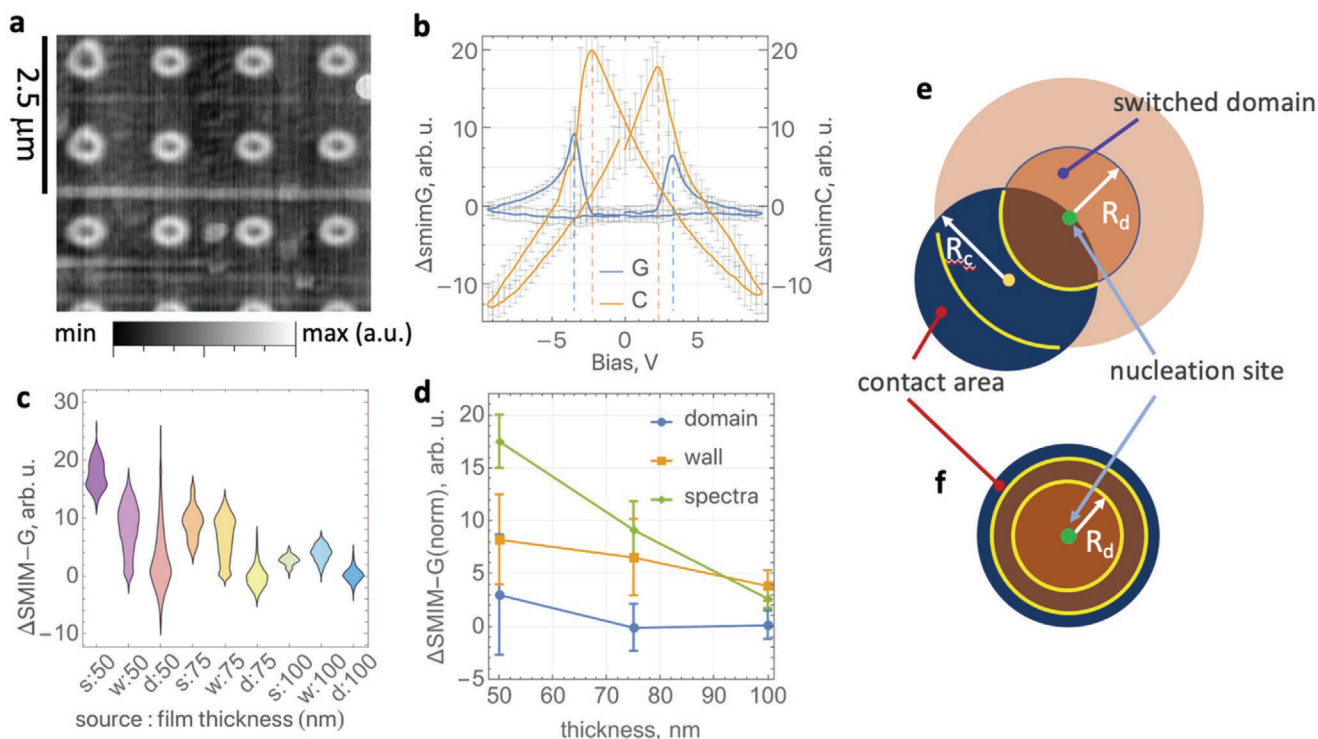


Figure 3. Microwave conductance of domain walls in PZT film with varying thicknesses. The original PZT film (native, 100 nm) was selectively sputtered by oxygen plasma (as discussed by Levlev et al.^[35]), creating regions with 75 and 50 nm nominal thickness. a) sMIM-G images of an array of nanodomains created by applying a DC pulse on a 4×4 point grid arrangement on the surface area of a plasma-etched 75 nm thick film. Owing to locally higher microwave conductance, the domain walls are clearly seen as “doughnut” shapes. b) Averaged sMIM-G and sMIM-C spectra collected from the triangular bias sweep (linear voltage ramps between -10 V and $+10$ V), of the 50 nm thick region. The spectra show ferroelectric switching, registered as peaks in conductivity (sMIM-G) as well as dielectric constant (sMIM-C). c) Statistics of thickness dependent microwave conductance of nanodomains. The “violin” diagram shows statistical distributions of the sMIM-G signals obtained by analysis of data presented in (a) and (b) from three etched areas with different thickness. The diagram compares contributions to the sMIM-G signal from domain walls measured by spectroscopy s:# (as presented in (b)), microscopy w:# (as presented in (a)), and the background signal away from the walls measured by microscopy d:#, where # refers to film thickness. d) Average values and standard deviations of the respective signals in (c) as a function of thickness. e) Schematic of the simplified geometric model of a nanodomain nucleating and growing in the contact area between the microwave probe and the ferroelectric film. The dark blue circle with the radius R_c is the tip-sample contact area; brown circle with the radius R_d and the light brown circle are a growing switched domain nucleated at the contact area boundary. The switched domain is represented by a circular cylinder for simplicity. f) The same as (e) for domain nucleated at the center of the contact area.

Meanwhile, the twofold change in observed conductance can be qualitatively explained by a simple geometrical model, which considers the length of the domain wall intersecting the microwave probe's contact area. Polarization reversal is initiated somewhere in the contact region between the probe and the surface. For simplicity, we can compare two representative scenarios: nucleation in the center of the contact region and nucleation at its periphery. A schematic of the model is shown in Figure 3e,f. In both cases, the growth of a reversed polarization domain above the switching voltage will initially increase the length of the domain wall that intersects the contact area, and subsequently decrease it once the domain expands beyond the contact. In the nucleation at the center of the contact area, the maximum length of the domain wall in the microwave contact is $2\pi R_c$, where R_c is the contact radius. The corresponding value for the nucleation at the periphery is $\approx 2.24R_c$. Our reference point in Figure 3e is the conductance of the straight segment of the domain wall (of macroscopically large domains in Figure 3a) scanned by the tip. The corresponding length of the domain wall segment in that case is $2R_c$. Therefore, we

expect a ratio of ≈ 2 – 3 between maximum conductance observed during switching and scanning, provided the conductance of the domain wall is the same in both cases. This is indeed quite close to the experimentally observed range in Figure 3b, and much smaller than the one-to-three orders of magnitude change of local conductance predicted by thermodynamic modeling as a function of domain-wall tilt.^[42] One possible reason is that tilted domain walls are intrinsically unstable, and even the presence of charge compensating mechanism will quickly diminish their angle to attain lower energy configuration. It is also possible that the wall conductance observed by sMIM requires the wall to make contact to the bottom electrode. In this case, likewise, we expect to observe only a moderate tilting angle of several degrees relative to the polar axis and a correspondingly weakly charged domain wall.^[30]

To extend this basic model, we utilized finite-element modeling of domain nucleation and growth, under a realistic-tip model with 100 nm contact radius. Although this contact area may be larger than those typically discussed for AFM tip-sample geometries, in the experiments we deliberately apply

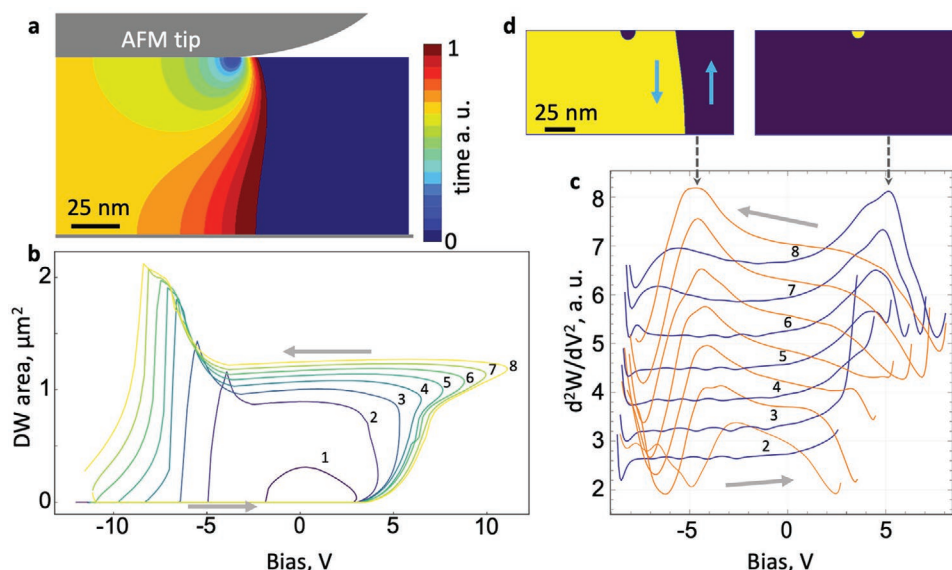


Figure 4. Finite element simulation of partial polarization switching driven by FORC bias waveform applied to the AFM tip. a) Evolution of domain shape evolution with linearly increasing bias. b) Total area of the domain walls as a function of FORC cycle defined by increasing value of positive turning voltage (cycle numbers are shown in the figure; arrows point to the direction of the voltage cycle). c) Second derivative of the domain wall energy d^2W/dV^2 for polarization configurations in (b) (the first cycle has been skipped for clarity). d) Domain configuration corresponding to peak values d^2W/dV^2 in cycle 8 of (c).

force to the tip in order to create a larger contact area. As seen in **Figure 4a**, in this case the domain nucleation does indeed initiate at the periphery of the contact, where the electric field is largest. Upon growth, the domain does not immediately obtain a cylindrical shape. Instead, it proceeds through stages in which it has the form of half-toroid, then dumbbell-like, and eventually cylindrical (see Figure S3 of the Supporting Information for additional details). As illustrated in **Figure 4b**, this shape progression involves an increase of the domain-wall area in the forward direction of the FORC waveform. However, the domain-wall area does not monotonously decrease in the reverse-switching direction. Instead it proceeds through initial increase of the total area (at ≈ -5 V) followed by a rapid decrease due to annihilation of the wall and reset to a domain-wall-free volume. This reverse transition is remarkably similar to the microwave conductance observed experimentally (**Figures 2b** and **3b**). Therefore, finite-element modeling provides one possible scenario for geometric variability of the domain-wall conductance, tied to evolution of domain-wall shape upon nucleation and subsequent growth.

A stronger connection of phase-field modeling to the experiment can be obtained by calculating the capacitance of the AFM junction. To this end, we estimated the capacitance of the volume incorporating the nanodomain via the 2nd derivative of the electrostatic energy (detailed in the Supporting Information). The dependence of small-signal capacitance on applied voltage calculated in this way (**Figure 4c**) is qualitatively reminiscent of the tunable capacitance–voltage characteristics measured experimentally (**Figure 3b**). According to the model, the capacitance is maximized around ± 5 V (**Figure 4c**). These values correspond to the onset of forward switching (yellow nucleus in **Figure 4d**) and the onset of reverse switching (purple nucleus in **Figure 4d**). This is

expected since the most polarizable ferroelectric state is the one where the applied field reduces the codirected polarization to its minimal value right before the initiation of the polarization switching. As a result, we claim that the capacitance peaks measured experimentally correspond to the threshold voltage of the initial stage of polarization switching, i.e., nucleation of a new nanodomain of opposite polarization. We can then also explain the peculiar synchronization between the sMIM-G and sMIM-C signals, observed on all the studied regions of the film. In particular, the peak of the sMIM-C signal precedes the peak of the sMIM-G signal in all switching spectra, as exemplified by **Figure 3b** (where the peak voltages in the sMIM-C are systematically smaller than in sMIM-G, see red dashed lines). The domain wall of the fresh nucleus does not traverse the film thickness (**Figure 4a,d**). As the nucleation progresses, the area of the domain wall increases, the capacitance of the junction drops, but the conductance starts to increase particularly when the domain wall traverses the volume of the film and makes contact to the bottom electrode (orange to red colors in **Figure 4a**). Therefore, within this interpretation, the peaks in the sMIM-C and sMIM-G signals essentially mark the onset of nucleation and the peak surface area of the domain wall. Finally, the increase of the peak sMIM-G signal with decreasing thickness also provides support for the basic picture of the domain wall as acting as a conductive filament connecting the top and bottom electrodes. In this case, the conductance of the filament will increase with decreasing film thickness, as is observed in **Figure 3b**. The role of the domain-wall curvature may also be present. However, AFM does not provide a direct estimate of domain wall curvature. This is an important avenue for future research to better understand the possible role of wall morphology and disorder in modulation of conductance.^[43]

3. Conclusions

To summarize, we have observed tunable microwave conductance associated with ferroelectric switching in a nanoscale contact geometry. The physical mechanism of tunable conductance is traced to the motion of the domain wall through the contact area, and the concomitant increase of the domain wall length in the contact. Nucleation and growth of nanodomains remains qualitatively similar from 25 to 100 nm film thickness. Such tunable junctions may provide an effective embodiment for neuromorphic circuitry that maintains highly resistive properties desired for ferroelectric switching, while allowing for tunable electronic read-out of the ferroelectric state. More generally, there will be additional contributions to tunable conductance arising from finite domain tilt or domain wall roughness. Such effects can feasibly be observed in thicker regions of the film where half-prolate domain nuclei with distinct domain wall curvature will be long-lived. Meanwhile, simultaneous piezoelectric and microwave conductance of growing nanodomains sheds new light on the nucleation and growth mechanisms, ultimately enabling new insight into motion of domain walls and the interaction of domain walls with the defects and interfaces.

4. Experimental Section

Thin Film Fabrication: Single-layer $\text{PbZr}_{0.2}\text{Ti}_{0.8}\text{O}_3$ thin films were synthesized using pulsed-laser deposition. The laser was a KrF excimer laser (248 nm, LPX 305, Coherent), in an on-axis geometry with a 60 mm target-to-substrate distance. Films were grown on 001-oriented SrTiO_3 single crystals attached to a resistive heater using Ag paint. SrRuO_3 bottom electrodes were grown from sintered ceramic targets at 100 mTorr of continuous O_2 , at 630 °C, at a fluence of 1.8 J cm^{-2} , and a frequency of 14 Hz. $\text{PbZr}_{0.2}\text{Ti}_{0.8}\text{O}_3$ was grown from a sintered $\text{Pb}_{1.1}\text{Zr}_{0.2}\text{Ti}_{0.8}\text{O}_3$ target at 200 mTorr of continuous O_2 , at 645 °C, at a fluence of 1.5 J cm^{-2} , and a frequency of 2 Hz. Following growth all films were cooled to room temperature in a static oxygen 760 mTorr environment at 5 °C min^{-1} .

sMIM/PFM Imaging and Spectroscopy: sMIM measurements were carried out through use of a ScanWave module (Prime Nano, Inc.) for Asylum MFP-3D atomic force microscope. The sMIM signal is comprised of the two parts of the complex admittance, $Y = G + jB$. Susceptance, B , is given by the capacitance times the applied AC frequency. The ScanWave module decouples the signal into sMIM-G (conductance) and sMIM-C (capacitance) signals. To calibrate the probe, the procedure of Huber et al. was followed,^[38] with measurements taken on a SiO_2 standard sample. Simultaneous sMIM and PFM were enabled through a bias-tee integrated in the ScanWave module. Images and spectra were collected through the Asylum AFM software. Further details on the sMIM experiment have been discussed by Tselev et al.^[30]

Finite Element Modeling: The details of finite element modeling using COMSOL are described in the Supporting Information.

Supporting Information

Supporting Information is available from the Wiley Online Library or from the author.

Acknowledgements

Experiments and modelling have been carried out at the Center for Nanophase Materials Sciences, Oak Ridge National Laboratory, which is a DOE Office of Science User Facility. This research was supported

in part by the Australian Research Council Centre of Excellence in Future Low-Energy Electronics Technologies (Project No. CE170100039) and funded by the Australian Government. This project was supported in part by an appointment to the Science Education and Workforce Development Programs at Oak Ridge National Laboratory, administered by ORISE through the U.S. Department of Energy Oak Ridge Institute for Science and Education. S.R.B. acknowledges funding in part from the UNSW Science Ph.D. Writing Scholarship and current funding from the Canada First Research Excellence Fund. In part (A.T.), this work was developed within the scope of the project CICECO-Aveiro Institute of Materials, UIDB/50011/2020 and UIDP/50011/2020, financed by national funds through the FCT/MEC and when appropriate cofinanced by FEDER under the PT2020 Partnership Agreement. J.C.A. acknowledges primary support from the National Science Foundation under grant TRIPODS+X: RES-1839234. L.W.M. acknowledges support of the National Science Foundation under Grant No. DMR-1708615. The authors would like to thank Liam Collins and Rama Vasudevan for assistance with the experimental set-up.

Conflict of Interest

The authors declare no conflict of interest.

Data Availability Statement

The data that support the findings of this study are available from the corresponding author upon reasonable request.

Keywords

domain wall conductance, lead zirconate titanate, scanning microwave impedance microscopy, scanning probe microscopy, thin film

Received: September 6, 2021

Revised: October 29, 2021

Published online: December 10, 2021

- [1] E. Y. Tsymlal, H. Kohlstedt, *Science* **2006**, 313, 181.
- [2] A. Gruverman, D. Wu, H. Lu, Y. Wang, H. W. Jang, C. M. Folkman, M. Y. Zhuravlev, D. Felker, M. Rzchowski, C. B. Eom, E. Y. Tsymlal, *Nano Lett.* **2009**, 9, 3539.
- [3] H. Yamada, V. Garcia, S. Fusil, S. Boyn, M. Marinova, A. Gloter, S. Xavier, J. Grollier, E. Jacquet, C. Carrétero, C. Deranlot, M. Bibes, A. Barthélémy, *ACS Nano* **2013**, 7, 5385.
- [4] A. Chanthbouala, A. Crassous, V. Garcia, K. Bouzehouane, S. Fusil, X. Moya, J. Allibe, B. Dlubak, J. Grollier, S. Xavier, C. Deranlot, A. Moshar, R. Proksch, N. D. Mathur, M. Bibes, A. Barthélemy, *Nat. Nanotechnol.* **2012**, 7, 101.
- [5] S. Boyn, J. Grollier, G. Lecerf, B. Xu, N. Locatelli, S. Fusil, S. Girod, C. Carrétero, K. Garcia, S. Xavier, J. Tomas, L. Bellaiche, M. Bibes, A. Barthélémy, S. Saïghi, V. Garcia, *Nat. Commun.* **2017**, 8, 14736.
- [6] P. Sharma, Q. Zhang, D. Sando, C. H. Lei, Y. Liu, J. Li, V. Nagarajan, J. Seidel, *Sci. Adv.* **2017**, 3, e1700512.
- [7] P. Sharma, D. Sando, Q. Zhang, X. Cheng, S. Prosandeev, R. Bulanadi, S. Prokhorenko, L. Bellaiche, L.-Q. Chen, V. Nagarajan, J. Seidel, *Adv. Funct. Mater.* **2019**, 29, 1807523.
- [8] H. Lu, Y. Tan, J. P. V. McConville, Z. Ahmadi, B. Wang, M. Conroy, K. Moore, U. Bangert, J. E. Shield, L.-Q. Chen, J. M. Gregg, A. Gruverman, *Adv. Mater.* **2019**, 0, 1902890.
- [9] J. P. V. McConville, H. Lu, B. Wang, Y. Tan, C. Cochard, M. Conroy, K. Moore, A. Harvey, U. Bangert, L.-Q. Chen, A. Gruverman, J. M. Gregg, *Adv. Funct. Mater.* **2020**, 30, 2000109.

- [10] A. Aird, E. K. H. Salje, *J. Phys.: Condens. Matter* **1998**, *10*, L377.
- [11] P. Maksymovych, S. Jesse, P. Yu, R. Ramesh, A. P. Baddorf, S. V. Kalinin, *Science* **2009**, *324*, 1421.
- [12] S. Farokhipoor, B. Noheda, *Phys. Rev. Lett.* **2011**, *107*, 127601.
- [13] J. Guyonnet, I. Gaponenko, S. Gariglio, P. Paruch, *Adv. Mater.* **2011**, *23*, 5377.
- [14] D. Meier, J. Seidel, A. Cano, K. Delaney, Y. Kumagai, M. Mostovoy, N. A. Spaldin, R. Ramesh, M. Fiebig, *Nat. Mater.* **2012**, *11*, 284.
- [15] J. Seidel, L. W. Martin, Q. He, Q. Zhan, Y. H. Chu, A. Rother, M. E. Hawkrig, P. Maksymovych, P. Yu, M. Gajek, N. Balke, S. V. Kalinin, S. Gemming, F. Wang, G. Catalan, J. F. Scott, N. A. Spaldin, J. Orenstein, R. Ramesh, *Nat. Mater.* **2009**, *8*, 229.
- [16] R. K. Vasudevan, Y. Matsumoto, X. Cheng, A. Imai, S. Maruyama, H. L. Xin, M. B. Okatan, S. Jesse, S. V. Kalinin, V. Nagarajan, *Nat. Commun.* **2014**, *5*, 4971.
- [17] A. Morelli, F. Johann, S. R. Burns, A. Douglas, J. M. Gregg, *Nano Lett.* **2016**, *16*, 5228.
- [18] N. Leo, A. Bergman, A. Cano, N. Poudel, B. Lorenz, M. Fiebig, D. Meier, *Nat. Commun.* **2015**, *6*, 6661.
- [19] J. T. Heron, J. L. Bosse, Q. He, Y. Gao, M. Trassin, L. Ye, J. D. Clarkson, C. Wang, J. Liu, S. Salahuddin, D. C. Ralph, D. G. Schlom, J. Iniguez, B. D. Huey, R. Ramesh, *Nature* **2014**, *516*, 370.
- [20] N. Balke, S. Choudhury, S. Jesse, M. Huijben, Y. H. Chu, A. P. Baddorf, L. Q. Chen, R. Ramesh, S. V. Kalinin, *Nat. Nanotechnol.* **2009**, *4*, 868.
- [21] S. S. P. Parkin, M. Hayashi, L. Thomas, *Science* **2008**, *320*, 190.
- [22] S. Manipatruni, D. E. Nikonov, C.-C. Lin, T. A. Gosavi, H. Liu, B. Prasad, Y.-L. Huang, E. Bonturim, R. Ramesh, I. A. Young, *Nature* **2019**, *565*, 35.
- [23] N. A. Benedek, T. Birol, *J. Mater. Chem. C* **2016**, *4*, 4000.
- [24] W. X. Zhou, *Jpn. J. Appl. Phys.* **2020**, *59*, S10802.
- [25] F. Y. Bruno, S. Boyn, S. Fusil, S. Girod, C. Carrétéro, M. Marinova, A. Gloter, S. Xavier, C. Deranlot, M. Bibes, A. Barthélémy, V. Garcia, *Adv. Electron. Mater.* **2016**, *2*, 1500245.
- [26] P. Chaudhary, H. Lu, A. Lipatov, Z. Ahmadi, J. P. V. McConville, A. Sokolov, J. E. Shield, A. Sinitskii, J. M. Gregg, A. Gruverman, *Nano Lett.* **2020**, *20*, 5873.
- [27] T. Sluka, A. K. Tagantsev, P. Bednyakov, N. Setter, *Nat. Commun.* **2013**, *4*, 1808.
- [28] J. Fujioka, A. Doi, D. Okuyama, D. Morikawa, T. Arima, K. N. Okada, Y. Kaneko, T. Fukuda, H. Uchiyama, D. Ishikawa, A. Q. R. Baron, K. Kato, M. Takata, Y. Tokura, *Sci. Rep.* **2015**, *5*, 13207.
- [29] X. Wu, U. Petralanda, L. Zheng, Y. Ren, R. Hu, S.-W. Cheong, S. Artyukhin, K. Lai, *Sci. Adv.* **2017**, *3*, e1602371.
- [30] A. Tselev, P. Yu, Y. Cao, L. R. Dedon, L. W. Martin, S. V. Kalinin, P. Maksymovych, *Nat. Commun.* **2016**, *7*, 11630.
- [31] Y.-L. Huang, L. Zheng, P. Chen, X. Cheng, S.-L. Hsu, T. Yang, X. Wu, L. Ponet, R. Ramesh, L.-Q. Chen, S. Artyukhin, Y.-H. Chu, K. Lai, *Adv. Mater.* **2020**, *32*, 1905132.
- [32] S. Cheng, Z. Fan, J. Rao, L. Hong, Q. Huang, R. Tao, Z. Hou, M. Qin, M. Zeng, X. Lu, G. Zhou, G. Yuan, X. Gao, J.-M. Liu, *iScience* **2020**, *23*, 101874.
- [33] A. R. Damodaran, S. Pandya, J. C. Agar, Y. Cao, R. K. Vasudevan, R. Xu, S. Saremi, Q. Li, J. Kim, M. R. McCarter, L. R. Dedon, T. Angsten, N. Balke, S. Jesse, M. Asta, S. V. Kalinin, L. W. Martin, *Adv. Mater.* **2017**, *29*, 1702069.
- [34] J. C. Agar, R. V. K. Mangalam, A. R. Damodaran, G. Velarde, J. Karthik, M. B. Okatan, Z. H. Chen, S. Jesse, N. Balke, S. V. Kalinin, L. W. Martin, *Adv. Mater. Interfaces* **2014**, *1*, 1400098.
- [35] A. V. Ievlev, C. Marius, N. L. Donovan, C. A. Joshua, A. V. Gabriel, W. M. Lane, V. K. Sergei, M. Petro, S. O. Olga, *Nanotechnology* **2018**, *29*, 155302.
- [36] R. Ramesh, *Spintronics IX* **2016**, 9931, 99312K.
- [37] X. Wu, K. Du, L. Zheng, D. Wu, S.-W. Cheong, K. Lai, *Phys. Rev. B* **2018**, *98*, 081409.
- [38] H. P. Huber, M. Moertelmaier, T. M. Wallis, C. J. Chiang, M. Hochleitner, A. Imtiaz, Y. J. Oh, K. Schilcher, M. Dieudonne, J. Smoliner, P. Hinterdorfer, S. J. Rosner, H. Tanbakuchi, P. Kabos, F. Kienberger, *Rev. Sci. Instrum.* **2010**, *81*, 113701.
- [39] K. Lai, W. Kundhikanjana, M. A. Kelly, Z.-X. Shen, *Appl. Nanosci.* **2011**, *1*, 13.
- [40] J. Shin, V. B. Nascimento, G. Geneste, J. Rundgren, E. W. Plummer, B. Dkhil, S. V. Kalinin, A. P. Baddorf, *Nano Lett.* **2009**, *9*, 3720.
- [41] P. Maksymovych, J. Seidel, Y. H. Chu, P. Wu, A. P. Baddorf, L. Q. Chen, S. V. Kalinin, R. Ramesh, *Nano Lett.* **2011**, *11*, 1906.
- [42] E. A. Eliseev, A. N. Morozovska, G. S. Svechnikov, P. Maksymovych, S. V. Kalinin, *Phys. Rev. B* **2012**, *85*, 045312.
- [43] L. Li, J. R. Jokisaari, Y. Zhang, X. Cheng, X. Yan, C. Heikes, Q. Lin, C. Cadre, D. G. Schlom, L.-Q. Chen, X. Pan, *Adv. Mater.* **2018**, *30*, 1802737.
- [44] A. N. Morozovska, A. V. Ievlev, V. V. Obukhovskii, Y. Fomichov, O. V. Varenyk, V. Y. Shur, S. V. Kalinin, E. A. Eliseev, *Phys. Rev. B* **2016**, *93*, 165439.
- [45] A. V. Ievlev, D. O. Alikin, A. N. Morozovska, O. V. Varenyk, E. A. Eliseev, A. L. Kholkin, V. Y. Shur, S. V. Kalinin, *ACS Nano* **2015**, *9*, 769.